

Pursuing 3D Scene Structures with Optical Satellite Images from Affine Reconstruction to Euclidean Reconstruction

Pinhe Wang, Limin Shi, Bao Chen, Zhanyi Hu, Qiulei Dong, and Jianzhong Qiao

Abstract—How to use multiple optical satellite images to recover the 3D scene structure is a challenging and important problem in the remote sensing field. Most existing methods in literature have been explored based on the classical RPC (rational polynomial camera) model which requires at least 39 GCPs (ground control points), however, it is not trivial to obtain such a large number of GCPs in many real scenes. Addressing this problem, we propose a hierarchical reconstruction framework based on multiple optical satellite images, which needs only 4 GCPs. The proposed framework is composed of an affine dense reconstruction stage and a followed affine-to-Euclidean upgrading stage: At the affine dense reconstruction stage, an affine dense reconstruction approach is explored for pursuing the 3D affine scene structure without any GCP from input satellite images. Then at the affine-to-Euclidean upgrading stage, the obtained 3D affine structure is upgraded to a Euclidean one with 4 GCPs. Experimental results on two public datasets demonstrate that the proposed method significantly outperforms three state-of-the-art methods in most cases.[1]

Index Terms—Optical satellite image, Affine dense reconstruction, RPC, GCPs, Affine-to-Euclidean upgrading.

I. INTRODUCTION

WITH the rapid development of the aerospace photography technology, an increasing number of high-resolution optical satellite images have been captured. In recent years, 3D scene reconstruction with optical satellite images, which aims to utilize multiple 2D scene images to automatically recover the corresponding 3D scene structure, has attracted more and more attention in both the fields of remote sensing and computer vision [2–17].

It is worth noting that although a large number of 3D reconstruction methods have been proposed in the computer vision field [18–23], most of them are generally available to handle the images captured by a plane array camera, but fail to straightforwardly handle the satellite images captured by a pushbroom camera where a linear sensor array is utilized to capture a line of imagery at a time, due to the fact that the imaging model of a linear pushbroom camera is quite distinct

from that of a plane array camera [24–27]. In the remote sensing field, existing sensor models are roughly divided in two categories [28]: physical models and generalized models. A physical model only represents the physical imaging process of a special sensor, but it is not available for handling the data from other sensors [29]. Generalized models utilize some general functions (e.g. polynomial function, rational function, etc.) to represent the functional relationship between the image space and the scene space, and they are able to effectively handle various sensor data [30, 31]. Hence, most of the recent 3D reconstruction methods with satellite optical images employ a generalized sensor model.

The RPC (rational polynomial camera) model [30] is a popular generalized sensor model, which is extensively used for 3D reconstruction with optical satellite images in literature [10, 13, 14]. Theoretically, it requires at least 39 uniformly distributed GCPs (ground control points) with accurate geographical coordinates to fit the RPC model, this is to say, these RPC-based reconstructions methods also have to use at least 39 GCPs during their reconstruction processes. However, since the scenes involved in optical satellite images are generally huge, it has to take a lot of time and effort to collect such GCPs, and the bigger the number of the collected GCPs is, the more laborious the GCPs collection is. This issue naturally raises the following problem: how to reconstruct 3D scenes based on optical satellite images by utilizing as few GCPs as possible?

Addressing this problem, we propose a hierarchical reconstruction framework based on multiple optical satellite images, which reconstructs the affine and Euclidean scene structures sequentially, called AE-Rec. At the first stage, we explore an affine dense reconstruction approach for obtaining the 3D affine structure from input satellite images, assuming that local small-sized tiles in satellite images is approximately subject to an affine camera model. This explored affine approach performs under a designed incremental reconstruction strategy, and it does not use any GCP. At the second stage, the obtained 3D affine structure is upgraded to a Euclidean one by fitting a global transformation matrix with at least 4 GCPs.

In sum, the main contributions in this paper include:

- 1 We explore a dense 3D affine reconstruction approach based on multiple satellite images, which employs an incremental reconstruction strategy to reconstruct affine scene structures without any GCP.
- 2 We propose the AE-Rec framework for 3D Euclidean

Pinhe Wang and Jianzhong Qiao are with the School of Computer Science and Engineering, University of Northeastern, Shenyang 110169, China.

Limin Shi is with the Research Center of Aerospace Information, Institute of Automation, Chinese Academy of Sciences, Beijing, 100190, China.

Bao Chen, Zhanyi Hu and Qiulei Dong are with the National Laboratory of Pattern Recognition, Institute of Automation, Chinese Academy of Sciences, Beijing, 100190, China, also with the School of Artificial Intelligence, University of Chinese Academy of Sciences, Beijing 100049, China, and also with the Center for Excellence in Brain Science and Intelligence Technology Chinese Academy of Sciences, Beijing 100190, China (e-mail: qldong@nlpr.ia.ac.cn)(Corresponding author: Qiulei Dong).

reconstruction based on optical satellite images, which could naturally accommodate the aforementioned 3D affine reconstruction approach. The proposed AE-Rec requires at least 4 GCPs, far less than the required minimum GCP number 39 by the existing RPC-based methods in literature [10, 13, 14]. Experimental results in Section IV further demonstrate that even if only 4 GCPs are used in the proposed AE-Rec, it still performs better than three comparative RPC-based methods in most cases.

The rest of this paper is organized as follows: Section II introduces related works. Our AE-Rec method is elaborated in Section III. Section IV reports the experimental results on two public datasets. Finally, some conclusions are drawn in Section V.

II. RELATED WORKS

In this section, we firstly give a brief introduction on the classical RPC model, considering that the RPC model has been widely used in many existing works [10, 14, 15, 32] for reconstructing 3D scene structures from satellite images in the remote sensing field. Then, we provide a review on existing 3D reconstruction methods based on optical satellite images.

A. RPC Model

In 1997, Hartley et al. [30] proposed an algorithm for estimating the parameters of the cubic rational polynomial camera which maps the image points as a rational polynomial function of world coordinates and it could model pushbroom cameras effectively. The frequently-used rational polynomial camera (RPC) model [33], which includes 78 coefficients and 10 normalized constants, is defined as:

$$\begin{aligned} r_n &= p_1(X_n, Y_n, Z_n) \\ c_n &= p_2(X_n, Y_n, Z_n), \end{aligned} \quad (1)$$

where r_n and c_n are the normalized row and column indices respectively, and $\{X_n, Y_n, Z_n\}$ denote the normalized coordinate values of object points in ground space, $\{p_i\}_{i=1}^2$ are ratios of two cubic polynomials parameterized by 39 coefficients [34]. Although the coefficients in the RPC model have no physical interpretation, it has become a standard practice for satellite image vendors to deliver an RPC model to accompany each satellite image, due to the fact that the RPC model has achieved high accuracies in all stages of the photogrammetry process just as performed by rigorous physical sensor models.

B. 3D Reconstruction Based on Optical Satellite Images

In the remote sensing field, most of the existing works for optical-image-based 3D reconstruction methods have been explored by utilizing the RPC model [10, 14, 15, 32]. With RPC model parameters provided, these methods usually focus on the minimum configuration of two-view stereo, and the general reconstruction flow involves (1) optimizing parameter

estimation residuals between the RPC models via block adjustment [35–39], (2) relying on disparity [10, 15, 32] or optical flow [14] to find dense correspondences between views, (3) performing triangulation based on RPC models to reconstruct the 3D scene structure corresponding to optical satellite images [40, 41]. Franchis et al. [13] proposed a fully automatic and modular stereo pipeline to produce digital elevation models from optical satellite images. This satellite stereo pipeline, abbreviated as s2p, replaced complicated non-linear bundle adjustment with relative pointing error correction between RPC models and recovers the 3D structure of pairwise satellite images by simple RPC-based elevation iteration. Facciolo et al. [42] analyzed the influences on two-view reconstruction, and proposed a novel RPC-based method. This method, which heuristically ranked all image pairs in the input set and then selectively merged the independent reconstructions generated by s2p [13], won the IARPA Multi-View Stereo 3D Mapping Challenge in 2016.

In addition to the aforementioned RPC-based methods, some works investigated the 3D reconstruction problem for optical satellite images. Fraser et al. [43] employed an affine model to reconstruct the 3D scene structure of entire satellite images, where the parameters of the affine model were calculated directly from the given ground control points. NASA Ames Research Center proposed the NASA Ames Stereo Pipeline, a suite of free and open source automated geodesy and stereogrammetry tools for processing stereo images captured from satellites (around Earth and other planets), where the rigorous physical sensor models used are obtained by querying ephemerides and interpolating camera pose [16]. Zhang et al. [17] adapted the state-of-the-art reconstruction pipeline COLMAP from the computer vision community to optical satellite image scenarios.

III. METHODOLOGY

In this section, we propose the AE-Rec framework for 3D Euclidean reconstruction based on optical satellite images. Firstly, we present the design motivation and pipeline of the AE-Rec framework, composed of an affine dense reconstruction stage and an affine-to-Euclidean upgrading stage. Then, we give detailed descriptions on the referred two stages respectively.

A. Design Motivation and Pipeline

As introduced above, the AE-Rec framework implements a 3D affine dense reconstruction firstly and then an affine-to-Euclidean upgrading, which is motivated by the following two points:

M1 It is noted that the imaging model of a pushbroom camera is essentially different from that of a plane array camera. However, a pushbroom camera (fixed on a satellite) moves approximately in a straight line in a short time, and the distance between the camera and the ground scene is enormous, hence, the mapping relationship between a small-sized tile in a satellite image and its corresponding 3D local scene could be modelled approximately by an affine camera model [44].

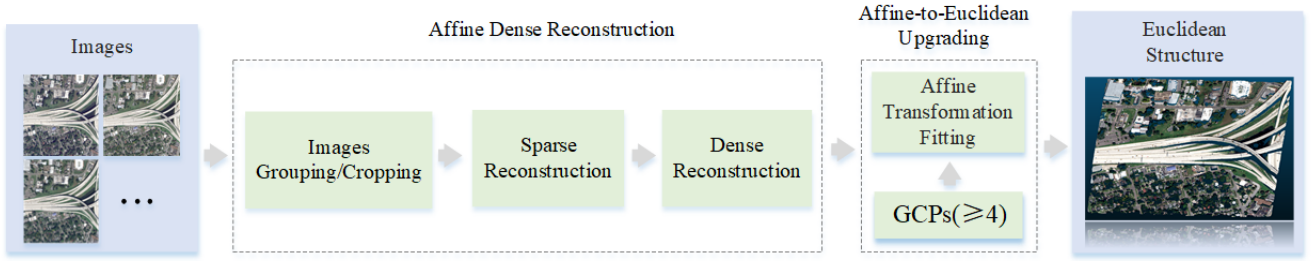


Fig. 1: AE-Rec framework.

M2 For a given set of satellite images, the calculated 3D affine structure under an affine camera model is up to an affine transformation in comparison to the corresponding Euclidean structure. This affine transformation matrix has 12 degrees of freedom, and it could be uniquely determined by at least 4 GCPs.

Based on the above two points, we design the pipeline of the proposed AE-Rec framework as shown in Fig. 1. As seen from this figure, the proposed method consists of two sequential stages, affine dense reconstruction and affine-to-Euclidean upgrading. Given a set of optical satellite images, they are cropped into a set of small-sized tiles, and these tiles are used to reconstruct an affine dense scene point cloud under an affine camera model based on the aforementioned motivation M1 at the affine dense reconstruction stage. Then at the affine-to-Euclidean stage, a global affine transformation matrix is fitted with at least 4 GCPs for upgrading the obtained 3D affine structure to a Euclidean based on the aforementioned motivation M2. In the following parts, the two stages will be described in detail.

B. Affine Dense Reconstruction Stage

In the affine dense reconstruction stage, a dense 3D affine reconstruction approach is explored for recovering the 3D scene structure from an input set of optical satellite images in an affine space under an incremental reconstruction strategy. The explored approach consists of three main steps as:

- S1 Image Grouping and Cropping: Considering that an arbitrary pair of images, which are captured for a same region with a relatively long time interval respectively, generally have much different textures for hampering accurate point matching, the input set of satellite images are firstly grouped into several subsets under an introduced image grouping criterion. Then, the grouped large-sized satellite images are cropped into numerous small-sized tiles with partial overlapping regions, so that these tiles could be effectively modeled by an affine camera model.
- S2 Sparse Reconstruction: For the tiles belong to each grouped subset of satellite images at Step S1, a high-quality point feature extraction/matching algorithm (here, SIFT [45] is straightforwardly used) is implemented for obtaining sparse point correspondences, and then a sparse affine reconstruction is implemented with these obtained point correspondences for obtaining a sparse affine scene structure and a set of affine camera motion matrices.

- S3 Dense Reconstruction: For each pair of tiles (belonging to an arbitrary grouped subsets of satellite images at Step S1) with overlapping regions, an affine stereo rectification is implemented, and then a stereo matching algorithm [46] is performed on these rectified tiles for obtaining dense feature correspondences. Both the obtained dense correspondences and affine camera motion matrices at Step S2 are jointly used for reconstructing a dense 3D affine structure.

Here, it has to be explained the reason of why the proposed affine dense reconstruction approach implements sparse reconstruction before dense reconstruction, rather than only implementing dense reconstruction: Generally compared with state-of-the-art sparse matching algorithms, the existing dense matching algorithms have a much larger number of point correspondences, but a lower matching accuracy. If the dense reconstruction is straightforwardly implemented by utilizing dense point correspondences (obtained by a dense matching algorithm) without a prior sparse reconstruction, the estimated global camera motion matrices would be relatively poorer due to the obtained point correspondences with a low matching accuracy, resulting in a relatively lower reconstruction accuracy. If a sparse reconstruction is implemented by utilizing sparse point correspondences (obtained by a sparse matching algorithm) before dense reconstruction, the estimated global camera motion matrices would be relatively better, resulting in a relatively better reconstruction accuracy.

In the following parts, we will give a detailed introduction to the above three steps:

1) *Image Grouping and Cropping*: As indicated above, an arbitrary pair of images that are captured for a same region with a relatively long time interval respectively, generally have much different textures for hampering accurate point matching. Hence, in input set of satellite images which are captured during a long time range, we introduce the following image grouping criterion to group the input set of images into several subsets: Images with capture time intervals less than 15 days are treated as the same grouped subset. In subsequent steps, we process each subset of optical satellite images independently.

Then, the large-sized satellite images in each subset are cropped into tiles with a same size $d \times d$ (d is much smaller than the size of the input images), subject to the condition that each pair of neighboring tiles have an overlapping regions with a size of $\frac{d}{3} \times d$ (or $d \times \frac{d}{3}$), as shown in Fig. 2. Since these tiles

are of a smaller size, they could be modeled approximately by an affine camera model. In addition, the overlapping regions belonging to neighboring tiles guarantee that the calculated local point clouds in the following sparse reconstruction step could be registered into a unified affine coordinate system.

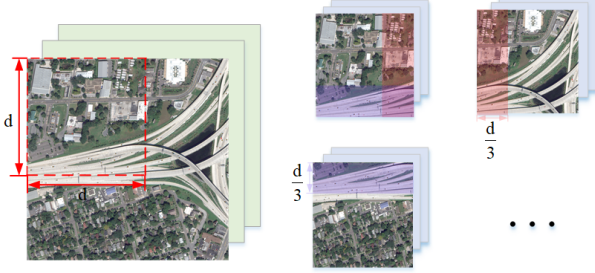


Fig. 2: Images cropping sample.

2) *Sparse Reconstruction*: Based on the obtained tiles above, a sparse reconstruction is implemented to estimate a set of global affine camera motion matrices in an incremental reconstruction strategy (as shown in Fig. 3), where an affine reconstruction of a selected initial pair of tiles is firstly built and then the other tiles are added iteratively to the reconstruction one at a time. This sparse reconstruction is built on the scene graph resulting from feature matching, and includes three main modules: affine reconstruction initialization, new tile addition, and local optimization.

Affine Reconstruction Initialization: Since all optical satellite images used in the affine dense reconstruction are captured over the same site, in order to obtain more robust and accurate reconstruction results, we select the initial image pair first, and then choose the initial tile pair used for the affine reconstruction initialization in the initial image pair. The sparser the matching points indicate that the angle between the two optical satellite images is larger, and such an image pair tends to obtain more accurate reconstruction results. Hence, we select the image pair with the sparsest SIFT matching as the initial image pair. In the initial image pair, we further separately count the number of matches in all small-sized tile pairs, and choose the small-sized tile pair with the largest SIFT matching number as the initial tile pair, which will ensure the quantity of reconstructed 3D points in the affine reconstruction initialization so that sufficient visible points are available for subsequent new tile additions.

With the aforementioned selected initial tile pair, we implement the affine reconstruction initialization using the factorization affine reconstruction algorithm [47]. Let Tile i and Tile j denote an arbitrary pair of tiles, which have a set of $n(\geq 4)$ correspondences $\{(\mathbf{x}_i^1, \mathbf{x}_j^1), \dots, (\mathbf{x}_i^k, \mathbf{x}_j^k), \dots, (\mathbf{x}_i^n, \mathbf{x}_j^n)\}$. \mathbf{x}_i^k and $\mathbf{x}_j^k \in \mathbb{R}^2$ ($k = 1, \dots, n$) represent the inhomogeneous coordinates of the k -th matching point in Tile i and Tile j respectively, and the inhomogeneous coordinates of their corresponding 3D point in the affine space is denoted as \mathbf{X}_{ij}^k . Let $A_i = [M_i, \mathbf{t}_i]$ and $A_j = [M_j, \mathbf{t}_j]$ denote the corresponding affine camera models to Tile i and Tile j respectively. As defined in [44], the mapping relationship between \mathbf{X}_{ij}^k and its

corresponding image point \mathbf{x}_i^k in Tile i (\mathbf{x}_j^k in Tile j) under the affine camera model A_i (also A_j) is formulate as:

$$\mathbf{x}_i^k = A_i[\mathbf{X}_{ij}^k; 1] = M_i\mathbf{X}_{ij}^k + \mathbf{t}_i. \quad (2)$$

Given a set of n correspondences between Tile i and Tile j , \mathbf{t}_i in A_i could be omitted by centralized the image points $\{\mathbf{x}_i^k\}_{k=1}^n$ into $\{\bar{\mathbf{x}}_i^k\}_{k=1}^n$ (i.e. $\{\bar{\mathbf{x}}_i^k\} = \{\mathbf{x}_i^k\} - 1/n \sum \mathbf{x}_i^k$), while \mathbf{t}_j could be omitted by centralized the image points $\{\bar{\mathbf{x}}_j^k\}_{k=1}^n$. Accordingly, the following constraint is obtained:

$$[\bar{\mathbf{x}}_i^k; \bar{\mathbf{x}}_j^k] = [M_i; M_j]\mathbf{X}_{ij}^k. \quad (3)$$

As noted from (3), once n is larger than 4, the affine space 3D points coordinates $\{\mathbf{X}_{ij}^k\}$ and the matrices $\{M_i, M_j\}$ could be obtained by minimizing the following objective functions:

$$\min_{M_i, M_j, \mathbf{X}_{ij}^k} \sum_k \|[\bar{\mathbf{x}}_i^k; \bar{\mathbf{x}}_j^k] - [M_i; M_j]\mathbf{X}_{ij}^k\|_F^2. \quad (4)$$

Here, a closed-form solution to the above minimization problem is simply obtained by SVD as indicated by matrix optimization theory [47]: if the SVD of matrix $W = UDV^T$, where W is a $4 \times n$ matrix formed by a set of n centralized correspondences,

$$W = \begin{bmatrix} \bar{\mathbf{x}}_i^1 & \dots & \bar{\mathbf{x}}_i^k & \dots & \bar{\mathbf{x}}_i^n \\ \bar{\mathbf{x}}_j^1 & \dots & \bar{\mathbf{x}}_j^k & \dots & \bar{\mathbf{x}}_j^n \end{bmatrix}. \quad (5)$$

then the product of the first three columns of U and the third-order submatrix in the upper left corner of D is $[M_i; M_j]$, and the 3D points coordinates \mathbf{X}_{ij}^k in affine space can be extracted from the first three columns of V . For more detail, refer to Algorithm 1.

New Tile Addition: Starting from the affine reconstruction initialization, the new tile addition is implemented by running two separate procedures of new tile registration and affine triangulation, alternatively. A new tile can be registered to the current affine 3D structure by using feature correspondences to reconstructed points in already registered tiles (2D-3D correspondences), thereby extending the set of reconstructed 3D points in the affine space through affine triangulation to increase scene coverage. The mapping relationship of affine camera model in (2) can be described in a more general form,

$$\begin{aligned} r_i^k &= A_i^1 X^k + A_i^2 Y^k + A_i^3 Z^k + A_i^4 \\ c_i^k &= A_i^5 X^k + A_i^6 Y^k + A_i^7 Z^k + A_i^8, \end{aligned} \quad (6)$$

where r_i^k and c_i^k are the row and column indices of the new tile image space point \mathbf{x}_i^k in a 2D-3D correspondence respectively, and (X^k, Y^k, Z^k) represents the coordinates of its corresponding 3D point in the current affine structure, A^1 to A^8 are the eight affine camera model parameters of the new tile. As can be seen from (6), these eight parameters per new tile require a set of $n(\geq 4)$ 2D-3D correspondences to be linearly solved. Due to the fact that 2D-3D correspondences are often contaminated with outliers, the RANSAC (random sample consistency) [48] algorithm is adopted for the robust estimation of the affine camera model parameters. Furthermore, we design a selection strategy to add new tile: there is no doubt that the tiles in the initial image pair are registered first according to the nearest-first principle, so that a global affine reconstruction structure about the initial image pair can

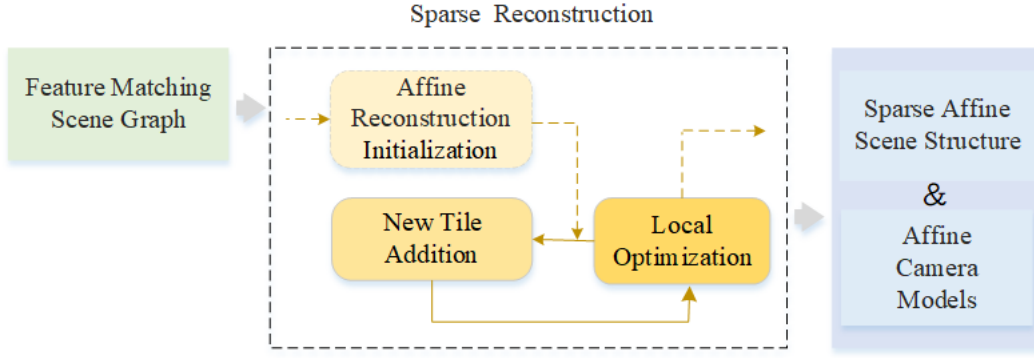


Fig. 3: Sparse reconstruction incremental strategy.

Algorithm 1 Affine Reconstruction Initialization [44].

Require:

Initial tiles pair correspondences $(\mathbf{x}_i^k, \mathbf{x}_j^k)$, $k = 1, \dots, n$;

Ensure:

Affine camera matrix $A_i = [M_i \ \mathbf{t}_i]$, $A_j = [M_j \ \mathbf{t}_j]$, and 3D points $\{\mathbf{X}_{i,j}^k\}$;

- 1: Compute translation vectors \mathbf{t}_i and \mathbf{t}_j , namely the centroid of points in Tile i (or Tile j),

$$\mathbf{t}_{i,j} = \frac{1}{n} \sum_k \mathbf{x}_{i,j}^k.$$

- 2: Centralized image point coordinates:

$$\{\bar{\mathbf{x}}_{i,j}^k\} = \{\mathbf{x}_{i,j}^k\} - \frac{1}{n} \sum_k \mathbf{x}_{i,j}^k,$$

- 3: Construct the $4 \times n$ matrix W from the centralized correspondence, and compute its SVD

$$W = UDV^\top.$$

- 4: Then the matrices $\{M_i, M_j\}$ are obtained from the product of first three columns of U and the first three singular values in D :

$$\begin{bmatrix} M_i \\ M_j \end{bmatrix} = [\sigma_1 \mathbf{u}_1 \ \sigma_2 \mathbf{u}_2 \ \sigma_3 \mathbf{u}_3].$$

and $\{\mathbf{X}_{i,j}^k\}$ are read from the first three columns of V

$$[\mathbf{X}_{i,j}^1 \ \dots \ \mathbf{X}_{i,j}^k \ \dots \ \mathbf{X}_{i,j}^n] = [\mathbf{v}_1 \ \mathbf{v}_2 \ \mathbf{v}_3]^\top.$$

be obtained. On this basis, we determine the order of adding new tiles according to the number of correspondences with the initial image pair as following the selection criteria for the initial tile pair.

A new 3D point can be affine triangulated and added to the global affine reconstruction points set as soon as a new tile covering the new scene is successfully registered. We implement the multi-view affine triangulation via the inverse of the affine camera matrix,

$$[\mathbf{X}^k; 1] = [A_1; \dots; A_i; \dots; A_n]^{-1} [\mathbf{x}_1^k; \dots; \mathbf{x}_i^k; \dots; \mathbf{x}_n^k], \quad (7)$$

where A_i denotes the affine camera model corresponding to each tile in the multi-view, and \mathbf{x}_i^k is the correspondence point which come from each tile, \mathbf{X}^k is the coordinate of the 3D point in the affine space obtained by affine triangulation. However, we perform triangulation only on the corresponding tiles from different images, to prevent redundant 3D points being reconstructed. Hence, we form feature tracks by concatenating the correspondences across corresponding tiles, and perform multi-view affine triangulation with these feature tracks.

Local Optimization: Without further refinement methods, the correspondences with noise will quickly propagate large errors during the iterations of tile registration and affine triangulation, resulting in the affine structure drifting to a non-recoverable state. We employ BA (Bundle Adjustment) [49] for the joint non-linear refinement of camera parameters A_i and 3D point parameters \mathbf{X}_i^k to minimize the affine reprojection error,

$$\min_{A_i, \mathbf{X}_i^k} \sum_i \sum_k \|\pi(A_i, \mathbf{X}_i^k) - \mathbf{x}_i^k\|_\gamma, \quad (8)$$

using a function π that projects 3D points in the affine space to image space and $\|\cdot\|_\gamma$ is a robust norm to potentially down-weight outliers. The optimization problems of bundle adjustments in affine reconstruction are solved with the Levenberg-Marquardt [50] algorithm implemented using Ceres [51].

3) *Dense Reconstruction:* In order to obtain dense point correspondences for reconstructing a dense affine structure, affine stereo rectification and stereo matching are performed sequentially on each pair of tiles with a sufficient number of sparse point correspondences. It is noted that the typical stereo rectification algorithms in literature [1, 52] are not available to handle large-sized satellite images which are generally captured by a pushbroom camera, hence, we introduce a local affine stereo rectification algorithm for re-projecting each pair of small-sized tiles to a new common plane parallel to the line between optical centers, which is outlined in Algorithm 2: given at least 4 correspondences from a tile pair, we estimate the affine fundamental matrix F_A between tiles in this pair employing the Gold Standard algorithm [44], and then two rectifying affine transformations are extracted from F_A [53], for rectifying the respective tiles. Once the pair of rectified tiles are obtained, MGM [46] is implemented on them for stereo matching, resulting in a set of dense point correspondences.

Algorithm 2 Affine stereo rectification [44, 53].

Require:

Tile i and Tile j , and their correspondences;

Ensure:

Rectified Tile i_{rect} and Tile j_{rect} ;

- 1: Estimate F_A by the Gold Standard algorithm;
 - 2: Extract H_i and H_j from F_A ;
 - 3: Rectify Tile i (Tile j) to Tile i_{rect} (Tile j_{rect}) with H_i (H_j) respectively.
-

After obtaining the dense correspondences and the global affine camera matrices, we use both of them jointly to reconstruct the dense 3D affine structure. For multi-view dense affine reconstruction, we transit the dense correspondences across multi-views to obtain dense matches tracks. Considering outliers and redundancies in the dense correspondence, a photometric consistency constraint is imposed on all dense matches tracks, which allows optimization to split tracks connected by weak correspondences, providing robustness to mismatches. Once all dense matches tracks are determined, we reconstruct the dense 3D point cloud in the affine space by multi-view affine triangulation in (7). Eventually, the 3D point coordinates of the dense affine reconstruction are optimized with BA to improve the geometric consistency of the global affine structure.

C. Euclidean Upgrading

It is noted that the obtained 3D scene structure at the above subsection is an affine structure, which is up to an affine transformation $H_A \in R^{4 \times 4}$ (under the homogeneous coordinate system) in comparison to the corresponding Euclidean structure:

$$H_A \mathbf{X}_A = \mathbf{X}_E, \quad (9)$$

where \mathbf{X}_A is an reconstructed 3D scene point in the affine coordinate system, and \mathbf{X}_E is the corresponding ground truth 3D point in the Euclidean coordinate system. Since the last row of an arbitrary affine transformation matrix with a size of 4×4 is $(0, 0, 0, 1)$, H_A has indeed 12 degrees of freedom, and it could be uniquely determined by at least 4 non-coplanar GCPs (with their corresponding image points) and their corresponding affine points which could be straightforwardly found according to the obtained mapping relationship between the tile image space and the affine space at Subsection B. In detail, assuming that $N (\geq 4)$ couples of GCPs in the Euclidean space and their corresponding points in the affine space are given. H_A is calculated by solving the following least-squares problem:

$$\min_{H_A} \sum_j \|H_A \mathbf{X}_A^j - \mathbf{X}_E^j\|_2^2. \quad (10)$$

In addition, when N is much larger than 4, RANSAC [48] could also be employed for achieving a more robust estimation by automatically removing possible outliers from the given couples of GCPs and their affine points.

D. Optional Post-processing

Since the input set of optical satellite images is grouped into several subsets (in Section B), our proposed AE-Rec framework reconstructs an independent Euclidean structure for each grouped subset. Although the different textures among the images in different subsets make the appearance changes among the Euclidean structures corresponding to these subsets. However, all images in these subsets cover the same geographic area, and if a more complete reconstruction is pursued, we perform optional post-processing on the reconstructed Euclidean structures corresponding to these subsets, i.e. utilizing the ICP (Iterative Closet Point) [54] algorithm to align and fuse several reconstructed Euclidean structures corresponding to the same geographic region.

IV. EXPERIMENTS

In this section, we evaluate the proposed AE-Rec method and three state-of-the-art methods, including JHU/APL method [14], S2P method [42], COLMAP method [17]. Firstly, we introduce two benchmark datasets and evaluation metrics. Then, we investigate the influence of image cropping size d on the reconstruction performance. Finally, the comparative evaluation on the proposed method and three state-of-the-art methods is implemented.

A. Datasets and Evaluation Metrics

To evaluate the effectiveness of our method, we conduct extensive experiments on the following two benchmark datasets:

- 1) MVS3DM Dataset[14]: MVS3DM dataset is provided by IARPA (Intelligence Advanced Research Projects Activity), which contains fifty WorldView-3 panchromatic, visible, and near infrared (VNIR) images, captured from November 2014 to January 2016 near San Fernando, Argentina. The ground truth DEM for evaluation was collected by airborne radar which ground sample distance (GSD) is approximately 30cm. Johns Hopkins University has preprocessed the dataset and identified eight reconstructable sites based on image overlap regions and LiDAR ranges.
- 2) DFC2019 Dataset[55]: DFC2019 dataset comes from the IEEE Geoscience and Remote Sensing (GRSS) Data Fusion Competition 2019. It consists of 2783 images from 106 observation sites corresponding to Jack Wilson, Florida, and Omaha, Nebraska. These WorldView-3 images were also collected from 2014 to 2016. The size is 2048×2048 for each RGB images, while the ground truth DSM size is 512×512 .

As done in [56], in order to evaluate the performances of all the comparative methods, we project the height values of the reconstructed 3D point clouds onto a normalized geographic grid by nearest-neighbor interpolation, with geographic grid units equal to the ground sample distance of ground truth DEMs in each dataset. The DEM generated by each comparative method are aligned to the ground-truth DEM, and the height values are compared pixel-wise to generate the height error maps. Then, the following two metrics are used for evaluation:

TABLE I: COMPLETENESS(%) AND ACCURACY(m) OF AE-REC WITH DIFFERENT IMAGE CROPPING SIZES

d	CP(%)	ME(m)
300	71.0	0.269
500	72.5	0.252
800	72.8	0.244
1000	72.9	0.239
1500	73.0	0.242
2000	72.2	0.240

- Median height error: the median value in the height error map;
- Completeness: the percentage of points with height error less than a threshold of 1m in the height error.

B. Influence of Image Cropping Size

We evaluate the influence of image cropping size d on the reconstruction performance by reconstructing two-views satellite images through the proposed method with $d = \{300, 500, 800, 1000, 1500, 2000\}$ respectively. The corresponding results are reported in Table 1. As seen from this table, the proposed method with $d = 1000$ achieve a trade-off among all the evaluation metrics, hence, this image cropping size d is always set to 1000 in all of our experiments. It is also noted that when d ranges from 800 to 2000, the corresponding results are quite close, demonstrating that the performance of the propose method is not sensitive to this image cropping size d in this range.

C. Comparison on Benchmark Data

Now, we evaluate our proposed method and compare it comprehensively with the experiment results of three state-of-the-art methods. Since both datasets were captured with a relatively long time interval, the optical satellite image set corresponding each site in both datasets can be grouped into several image subsets. For the sake of fairness, the comparison experiments will be conducted in two parts. First, we evaluate the accuracy and completeness of the aforementioned methods using the selected subsets of images corresponding to each site in both datasets. And then, the reconstruction performance and run-time of these methods are evaluated in the complete image set of these sites.

1) *For the selected image subset:* Here, we report the evaluation results for 15 sites in the aforementioned two datasets. Among them, 8 sites are from the MVS3DM dataset and the image subsets of these sites are provided by Johns Hopkins University (containing 3-4 images). The other 7 sites are from the DFC2019 dataset, and the image subset corresponding to each site is the largest subset selected according to the image grouping method described above (containing 5-8 images). The evaluation results for the two datasets are presented in Table 2 and Table 3, respectively, and we observe that the proposed AE-Rec framework outperforms the other three state-of-the-art methods. It ensure that the reconstructed DSMs obtain the highest completeness while maintaining the lowest median height error among all methods, which is consistent

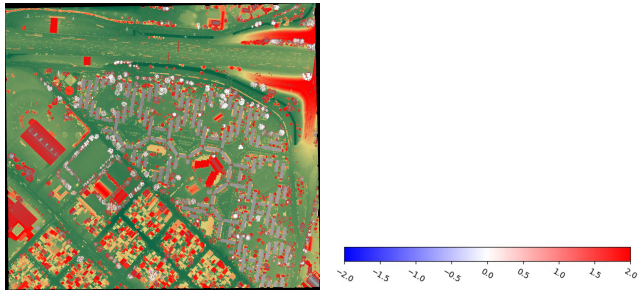
TABLE II: COMPARISON OF QUANTITATIVE RESULTS ON SELECTED SUBSETS OF MVS3DM DATASET.

MVS3DM	Method	CP(%)	ME(m)
Site1	JHU/APL[14]	64.0	0.577
	COLMAP[17]	61.7	0.276
	S2P[56]	72.4	0.319
	Ours	74.7	0.259
Site2	JHU/APL[14]	62.3	0.597
	COLMAP[17]	63.1	0.302
	S2P[56]	67.1	0.340
	Ours	70.9	0.302
Site3	JHU/APL[14]	52.9	0.614
	COLMAP[17]	31.9	0.364
	S2P[56]	63.6	0.392
	Ours	65.7	0.345
Site4	JHU/APL[14]	39.7	1.346
	COLMAP[17]	10.9	0.632
	S2P[56]	40.6	0.380
	Ours	41.8	0.363
Site5	JHU/APL[14]	70.3	0.389
	COLMAP[17]	62.4	0.312
	S2P[56]	67.2	0.369
	Ours	71.4	0.272
Site6	JHU/APL[14]	66.6	0.442
	COLMAP[17]	58.9	0.323
	S2P[56]	64.6	0.381
	Ours	67.8	0.283
Site7	JHU/APL[14]	49.9	0.916
	COLMAP[17]	33.9	0.373
	S2P[56]	48.5	0.317
	Ours	50.1	0.298
Site8	JHU/APL[14]	54.3	0.601
	COLMAP[17]	20.0	0.452
	S2P[56]	51.0	0.322
	Ours	51.7	0.320

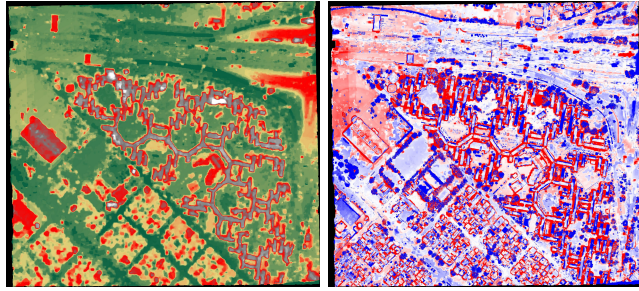
TABLE III: COMPARISON OF QUANTITATIVE RESULTS ON SELECTED SUBSETS OF DFC2019 DATASET.

DFC2019	Method	CP(%)	ME(m)
Site1	JHU/APL[14]	2.0	14.070
	COLMAP[17]	51.3	0.443
	S2P[56]	76.8	0.267
	Ours	82.1	0.235
Site2	JHU/APL[14]	64.9	0.603
	COLMAP[17]	45.1	0.344
	S2P[56]	68.2	0.462
	Ours	72.1	0.337
Site3	JHU/APL[14]	55.9	0.814
	COLMAP[17]	41.4	0.451
	S2P[56]	65.7	0.223
	Ours	67.7	0.186
Site4	JHU/APL[14]	69.8	0.450
	COLMAP[17]	57.5	0.349
	S2P[56]	72.2	0.330
	Ours	73.9	0.216
Site5	JHU/APL[14]	72.2	0.344
	COLMAP[17]	33.4	0.224
	S2P[56]	77.8	0.162
	Ours	78.4	0.141
Site6	JHU/APL[14]	72.7	0.279
	COLMAP[17]	52.5	0.245
	S2P[56]	80.4	0.183
	Ours	82.6	0.148
Site7	JHU/APL[14]	93.0	0.129
	COLMAP[17]	73.9	0.112
	S2P[56]	96.4	0.076
	Ours	96.5	0.072

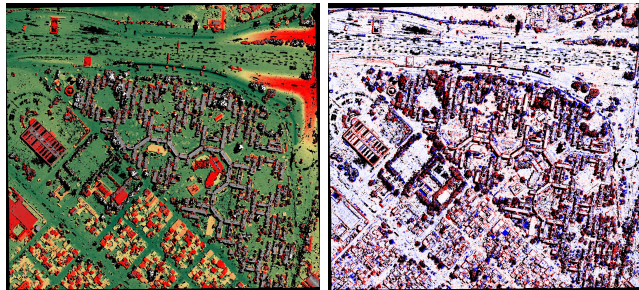
with the visualization of the height error maps in Fig. 4 and Fig. 5.



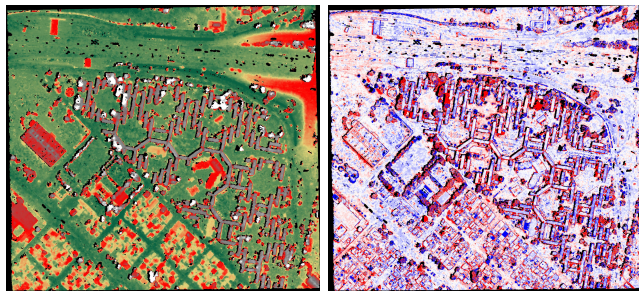
(a) Ground-Truth & COLOR BAR



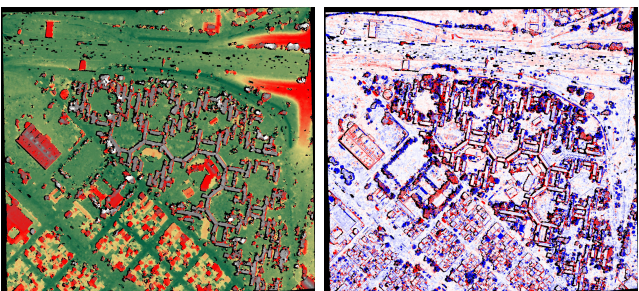
(b) JHU/APL[14]



(c) COLMAP[17]

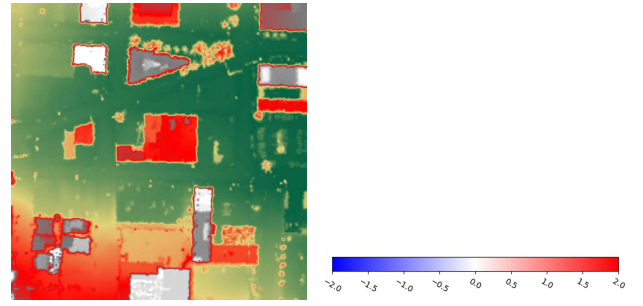


(d) S2P17[42]

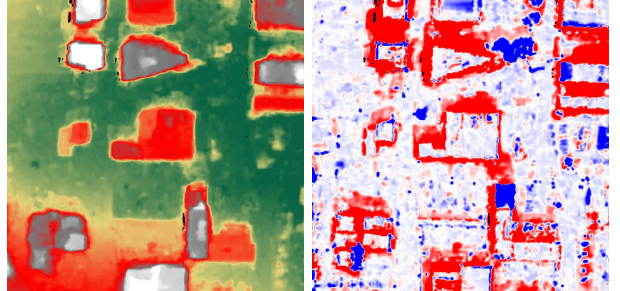


(e) Ours

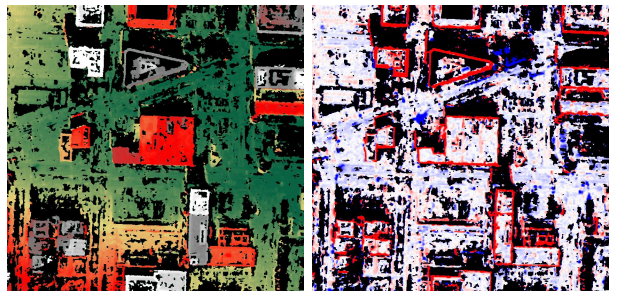
Fig. 4: HEIGHT ERROR MAPS ON SITE 1 OF MVS3DM DATASET.



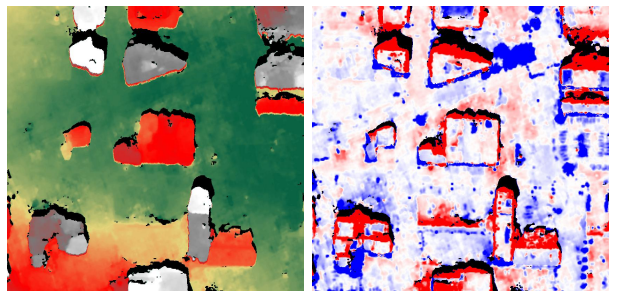
(a) Ground-Truth & COLOR BAR



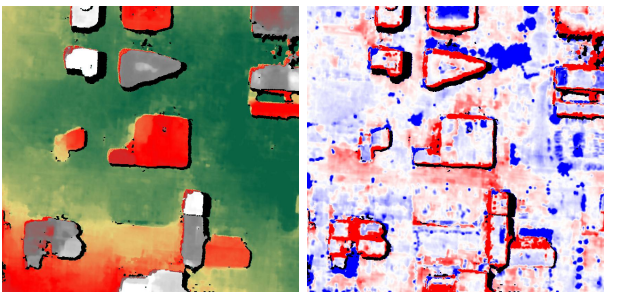
(b) JHU/APL[14]



(c) COLMAP[17]



(d) S2P17[42]



(e) Ours

Fig. 5: HEIGHT ERROR MAPS ON SITE 6 OF DFC2019 DATASET.

TABLE IV: COMPARISON OF QUANTITATIVE RESULTS ON COMPLETE SETS OF MVS3DM DATASET.

MVS3DM	Method	CP(%)	ME(m)	Time(mins)
Site1	JHU/APL[14]	72.4	0.324	151.5
	COLMAP[17]	72.5	0.315	86.7
	S2P[56]	80.1	0.317	70.1
	Ours	81.4	0.215	91.3
Site2	JHU/APL[14]	70.4	0.391	147.9
	COLMAP[17]	66.8	0.450	83.8
	S2P[56]	74.0	0.486	71.4
	Ours	75.7	0.345	88.2
Site3	JHU/APL[14]	59.7	0.594	127.1
	COLMAP[17]	63.4	0.393	50.7
	S2P[56]	73.1	0.524	43.8
	Ours	74.1	0.379	59.5
Site4	JHU/APL[14]	43.9	1.346	119.2
	COLMAP[17]	50.0	1.632	48.9
	S2P[56]	58.6	1.091	42.1
	Ours	60.8	0.856	53.9

2) *For the complete image set:* In addition, we also report comparative evaluation on the complete image sets corresponding to the first 4 sites in the MVS3DM dataset. Our proposed method performs optional post-processing of image set for each site, and the other three state-of-the-art methods all have their own fusion strategies. As shown in Table 4, our proposed method wins again in the comparison of the reconstruction performance for the entire image set in each site, which is consistent with the evaluation results in Table 2. This is attributed to the fact that our proposed method employs an affine camera model to approximate the small-sized tile in optical satellite image, which not only increase the accuracy of the camera model approximation, but also enables many optimization methods in computer vision filed to be directly applied to our proposed AE-Rec framework. Moreover, the image grouping strategy we designed works well.

However, as can be seen from the last column of Table 4, our proposed method costs more time compared to S2P and COLMAP methods, which is due that we employ an incremental reconstruction strategy in the affine dense reconstruction stage, and thus the iterative local optimization consumes a lot of computation time. S2P [42] takes the shortest run-time among these methods because it performs only simple linear optimization during the reconstruction. COLMAP [17] run faster than our proposed method in that it only adjusts the position of the principal point in the camera model during bundle adjustment (BA). JHU/APL [14] involves solving non-trivial third-order polynomial systems during the RPC model optimization, so it takes the longest run-time. It is necessary to state here that the aforementioned run-time are counted with the RPC model known without considering the run-time required for GCPs collection and RPC model fitting. Otherwise, our method still offers advantages in terms of efficiency.

V. CONCLUSION

In this paper, for the problem of how to recover the 3D scene structure from optical satellite images using as few GCPs as possible, we propose the AE-Rec method, which consists of two stages: affine reconstruction and affine-to-Euclidean upgrading. Unlike most RPC model-based methods, our method

enables to recover the Euclidean structure of multiple optical satellite images with at least 4 GCPs. Experimental results on the MVS3DM and DFC2019 datasets demonstrate the advantages of our method compared to the three state-of-the-art optical satellite image 3D reconstruction methods.

In future, we will investigate how to effectively utilize the semantic information in optical satellite images to obtain semantic 3D reconstruction with optical satellite images, and improve the reconstruction accuracy of our proposed AE-Rec framework based on the consistency in the semantic information between images.

REFERENCES

- [1] Y. Ohta and T. Kanade, "Stereo by intra- and inter-scanline search using dynamic programming," *IEEE Transactions on Pattern Analysis and Machine Intelligence*, vol. PAMI-7, no. 2, pp. 139–154, 1985.
- [2] Y. Ye, L. Bruzzone, J. Shan, F. Bovolo, and Q. Zhu, "Fast and robust matching for multimodal remote sensing image registration," *IEEE Transactions on Geoscience and Remote Sensing*, vol. 57, no. 11, pp. 9059–9070, 2019.
- [3] G. Xiao, H. Luo, K. Zeng, L. Wei, and J. Ma, "Robust feature matching for remote sensing image registration via guided hyperplane fitting," *IEEE Transactions on Geoscience and Remote Sensing*, pp. 1–14, 2020.
- [4] J. Li, Q. Hu, and M. Ai, "Robust geometric model estimation based on scaled welsch ℓ_1 -norm," *IEEE Transactions on Geoscience and Remote Sensing*, vol. 58, no. 8, pp. 5908–5921, 2020.
- [5] J. Liu, W. Xu, B. Guo, G. Zhou, and H. Zhu, "Accurate mapping method for uav photogrammetry without ground control points in the map projection frame," *IEEE Transactions on Geoscience and Remote Sensing*, vol. 59, no. 11, pp. 9673–9681, 2021.
- [6] S. Gholinejad, A. A. Naeini, and A. Amiri-Simkooei, "Optimization of rfm problem using linearly programmed ℓ_1 -regularization," *IEEE Transactions on Geoscience and Remote Sensing*, vol. PP, no. 99, pp. 1–9, 2021.
- [7] S. Chen, J. Chen, Z. Xiong, L. Xing, Y. Yang, F. Xiao, K. Yan, and H. Li, "Learning relaxed neighborhood consistency for feature matching," *IEEE Transactions on Geoscience and Remote Sensing*, pp. 1–13, 2021.
- [8] D. He, Q. Shi, X. Liu, Y. Zhong, and X. Zhang, "Deep subpixel mapping based on semantic information modulated network for urban land use mapping," *IEEE Transactions on Geoscience and Remote Sensing*, pp. 1–19, 2021.
- [9] J. Wohlfeil, H. Hirschmüller, B. Piltz, A. Börner, and M. Suppa, "Fully automated generation of accurate digital surface models with sub-meter resolution from satellite imagery," *Int. Arch. Photogramm. Rem. Sens. Spatial Inf. Sci.*, pp. 34–B3, 2012.
- [10] P. d'Angelo and P. Reinartz, "Dsm based orientation of large stereo satellite image blocks," *Int. Arch. Photogramm. Rem. Sens. Spatial Inf. Sci.*, vol. 39, no. B1, pp. 209–214, 2012.

- [11] P. d'Angelo and G. Kuschik, "Dense multi-view stereo from satellite imagery," in *IEEE International Geoscience and Remote Sensing Symposium (IGARSS)*, pp. 6944–6947, 2012.
- [12] G. Kuschik, "Large scale urban reconstruction from remote sensing imagery," *International Archives of the Photogrammetry, Remote Sensing and Spatial Information Sciences*, vol. 5, no. W1, p. 1, 2013.
- [13] C. De Franchis, E. Meinhardt-Llopis, J. Michel, J. M. Morel, and G. Facciolo, "An automatic and modular stereo pipeline for pushbroom images," in *ISPRS Annals of the Photogrammetry, Remote Sensing and Spatial Information Sciences*, vol. II-3, pp. 49–56, 2014.
- [14] M. Bosch, Z. Kurtz, S. Hagstrom, and M. Brown, "A multiple view stereo benchmark for satellite imagery," in *IEEE Applied Imagery Pattern Recognition Workshop (AIPR)*, pp. 1–9, 2016.
- [15] D. E. Shean, O. Alexandrov, Z. M. Moratto, B. E. Smith, I. R. Joughin, C. Porter, and P. Morin, "An automated, open-source pipeline for mass production of digital elevation models (dems) from very-high-resolution commercial stereo satellite imagery," *ISPRS Journal of Photogrammetry and Remote Sensing*, vol. 116, pp. 101–117, 2016.
- [16] R. A. Beyer, O. Alexandrov, and S. McMichael, "The ames stereo pipeline: Nasa's open source software for deriving and processing terrain data," *Earth and Space Science*, vol. 5, no. 9, pp. 537–548, 2018.
- [17] K. Zhang, N. Snavely, and J. Sun, "Leveraging vision reconstruction pipelines for satellite imagery," in *Proceedings of the IEEE/CVF International Conference on Computer Vision (ICCV) Workshops*, Oct 2019.
- [18] M. Jancosek and T. Pajdla, "Multi-view reconstruction preserving weakly-supported surfaces," in *Proceedings of the IEEE Conference on Computer Vision and Pattern Recognition (CVPR)*, pp. 3121–3128, 2011.
- [19] S. Fuhrmann, F. Langguth, and M. Goesele, "Mve - a multi-view reconstruction environment," in *Eurographics Workshop on Graphics and Cultural Heritage (GCH)*, pp. 11–18, 2014.
- [20] J. L. Schönberger, E. Zheng, M. Pollefeys, and J. M. Frahm, "Pixelwise view selection for unstructured multi-view stereo," in *European Conference on Computer Vision (ECCV)*, pp. 501–518, 2016.
- [21] Q. Dong, M. Shu, H. Cui, H. Xu, and Z. Hu, "Learning stratified 3d reconstruction," *Science China Information Sciences*, vol. 61, no. 2, pp. 220–235, 2018.
- [22] Q. Dong and H. Wang, "Latent-smoothness nonrigid structure from motion by revisiting multilinear factorization," *IEEE Transactions on Cybernetics*, vol. 49, no. 9, pp. 3557–3570, 2019.
- [23] Q. Dong, X. Gao, H. Cui, and Z. Hu, "Robust camera translation estimation via rank enforcement," *IEEE Transactions on Cybernetics*, pp. 1–11, 2020.
- [24] G. Konecny, "Evaluation of spot imagery on analytical photogrammetric instruments," *Photogrammetric Engineering and Remote Sensing*, vol. 53, pp. 1223–1230, 1987.
- [25] D. J. Gagan and I. J. Dowman, "Accuracy and completeness of topographic mapping from spot imagery," *The Photogrammetric Record*, vol. 12, no. 72, pp. 787–796, 1988.
- [26] T. Kim, "A study on the epipolarity of linear pushbroom images," *Photogrammetric engineering and remote sensing*, vol. 66, no. 8, pp. 961–966, 2000.
- [27] A. F. Habib, M. Morgan, S. Jeong, and K. O. Kim, "Analysis of epipolar geometry in linear array scanner scenes," *The Photogrammetric Record*, vol. 20, no. 109, pp. 27–47, 2005.
- [28] C. V. Tao and Y. Hu, "A comprehensive study of the rational function model for photogrammetric processing," *Photogrammetric engineering and remote sensing*, vol. 67, no. 12, pp. 1347–1358, 2001.
- [29] H. Hirschmüller, F. Scholten, and G. Hirzinger, "Stereo vision based reconstruction of huge urban areas from an airborne pushbroom camera (hrsc)," in *Joint Pattern Recognition Symposium*, pp. 58–66, 2005.
- [30] R. I. Hartley and T. Saxena, "The cubic rational polynomial camera model," in *Image Understanding Workshop*, vol. 649, p. 653, 1997.
- [31] R. Gupta and R. I. Hartley, "Linear pushbroom cameras," *IEEE Transactions on Pattern Analysis and Machine Intelligence*, vol. 19, no. 9, pp. 963–975, 1997.
- [32] E. Rupnik, M. Daakir, and M. P. Deseilligny, "Micmac—a free, open-source solution for photogrammetry," *Open Geospatial Data, Software and Standards*, vol. 2, no. 1, pp. 1–9, 2017.
- [33] Y. Hu, V. Tao, and A. Croitoru, "Understanding the rational function model: methods and applications," *International archives of photogrammetry and remote sensing*, vol. 20, no. 6, pp. 119–124, 2004.
- [34] T. Toutin, "Geometric processing of remote sensing images: models, algorithms and methods," *International journal of remote sensing*, vol. 25, no. 10, pp. 1893–1924, 2004.
- [35] H. B. Hanley, T. Yamakawa, and C. S. Fraser, "Sensor orientation for high-resolution satellite imagery," *International Archives of Photogrammetry Remote Sensing and Spatial Information Sciences*, vol. 34, no. 1, pp. 69–75, 2002.
- [36] H. B. Hanley and C. S. Fraser, "Sensor orientation for high-resolution satellite imagery: Further insights into bias-compensated rpcs," in *XX. Congress of International Society for Photogrammetry and Remote Sensing (ISPRS), Commission I, Working Group I/2*, pp. 12–23, 2004.
- [37] C. S. Fraser and H. B. Hanley, "Bias-compensated rpcs for sensor orientation of high-resolution satellite imagery," *Photogrammetric Engineering and Remote Sensing*, vol. 71, no. 8, pp. 909–915, 2005.
- [38] J. Grodecki and G. Dial, "Block adjustment of high-resolution satellite images described by rational polynomials," *Photogrammetric Engineering and Remote Sensing*, vol. 69, no. 1, pp. 59–68, 2003.
- [39] C. de Franchis, E. Meinhardt-Llopis, J. Michel, J. M. Morel, and G. Facciolo, "On stereo-rectification of push-

- broom images,” in *IEEE International Conference on Image Processing (ICIP)*, pp. 5447–5451, 2014.
- [40] C. V. Tao and Y. Hu, “3d reconstruction methods based on the rational function model,” *Photogrammetric engineering and remote sensing*, vol. 68, no. 7, pp. 705–714, 2002.
- [41] E. Zheng, K. Wang, E. Dunn, and J. Frahm, “Minimal solvers for 3d geometry from satellite imagery,” in *Proceedings of the IEEE International Conference on Computer Vision*, pp. 738–746, 2015.
- [42] G. Facciolo, C. De Franchis, and E. Meinhardt-Llopis, “Automatic 3d reconstruction from multi-date satellite images,” in *Proceedings of the IEEE Conference on Computer Vision and Pattern Recognition Workshops*, pp. 57–66, 2017.
- [43] C. S. Fraser, P. M. Dare, and T. Yamakawa, “Digital surface modelling from spot 5 hrs imagery using the affine projective model,” in *International Society for Photogrammetry and Remote Sensing (ISPRS) Congress*, vol. 35, pp. 385–388, 2004.
- [44] R. Hartley and A. Zisserman, “Multiple view geometry in computer vision,” 2003.
- [45] D. G. Low, “Distinctive image features from scale-invariant keypoints,” *International Journal of Computer Vision*, vol. 60, no. 2, pp. 91–110, 2004.
- [46] G. Facciolo, C. De Franchis, and E. Meinhardt, “Mgm: A significantly more global matching for stereovision,” in *British Machine Vision Conference (BMVC)*, 2015.
- [47] C. Tomasi and T. Kanade, “Shape and motion from image streams under orthography: A factorization approach,” *International Journal of Computer Vision*, vol. 9, no. 2, pp. 137–154, 1992.
- [48] M. A. Fischler and R. C. Bolles, “Random sample consensus: a paradigm for model fitting with applications to image analysis and automated cartography,” *Communications of the ACM*, vol. 24, no. 6, pp. 381–395, 1981.
- [49] B. Triggs, “Bundle adjustment – a modern synthesis,” *Springer-Verlag*, 1999.
- [50] K. Levenberg, “A method for the solution of certain non-linear problems in least squares,” *Quarterly of applied mathematics*, vol. 2, no. 2, pp. 164–168, 1944.
- [51] S. Agarwal, K. Mierle, and Others, “Ceres solver.” <http://ceres-solver.org>.
- [52] A. Fusiello, E. Trucco, and A. Verri, “A compact algorithm for rectification of stereo pairs,” *Machine vision and applications*, vol. 12, no. 1, pp. 16–22, 2000.
- [53] C. Loop and Z. Z., “Computing rectifying homographies for stereo vision,” in *Proceedings. 1999 IEEE Computer Society Conference on Computer Vision and Pattern Recognition (Cat. No PR00149)*, vol. 1, pp. 125–131, 1999.
- [54] K. S. Arun, “Least-squares fitting of two 3-d point sets,” *IEEE Trans Pattern Anal Mach Intell*, vol. 9, no. 5, pp. 698–700, 1987.
- [55] M. Bosch, K. Foster, G. Christie, S. Wang, G. D. Hager, and M. Brown, “Semantic stereo for incidental satellite images,” in *IEEE Winter Conference on Applications of Computer Vision (WACV)*, pp. 1524–1532, 2019.
- [56] M. Bosch, A. Leichtman, D. Chilcott, H. Goldberg, and M. Brown, “Metric evaluation pipeline for 3d modeling of urban scenes,” *International Archives of the Photogrammetry, Remote Sensing and Spatial Information Sciences (ISPRS)*, vol. 42, pp. 239–246, 2017.